

# Highly Selective On-Surface Ring-Opening of Aromatic Azulene Moiety

Lulu Wang,<sup>#</sup> Xinnan Peng,<sup>#</sup> Jie Su,<sup>#</sup> Junting Wang,<sup>#</sup> Aurelio Gallardo, Hui Yang, Qifan Chen, Pin Lyu, Pavel Jelínek,\* Junzhi Liu,\* Ming Wah Wong,\* and Jiong Lu\*



Cite This: *J. Am. Chem. Soc.* 2024, 146, 1563–1571



Read Online

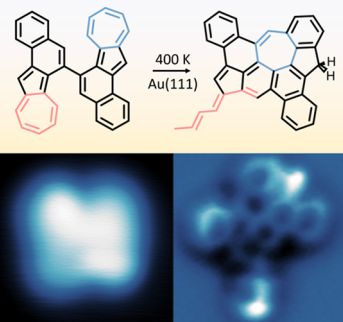
ACCESS |

Metrics & More

Article Recommendations

Supporting Information

**ABSTRACT:** Controllable ring-opening of polycyclic aromatic hydrocarbons plays a crucial role in various chemical and biological processes. However, breaking down aromatic covalent C–C bonds is exceptionally challenging due to their high stability and strong aromaticity. This study presents a seminal report on the precise and highly selective on-surface ring-opening of the seven-membered ring within the aromatic azulene moieties under mild conditions. The chemical structures of the resulting products were identified using bond-resolved scanning probe microscopy. Furthermore, through density functional theory calculations, we uncovered the mechanism behind the ring-opening process and elucidated its chemical driving force. The key to achieving this ring-opening process lies in manipulating the local aromaticity of the aromatic azulene moiety through strain-induced internal ring rearrangement and cyclo-dehydrogenation. By precisely controlling these factors, we successfully triggered the desired ring-opening reaction. Our findings not only provide valuable insights into the ring-opening process of polycyclic aromatic hydrocarbons but also open up new possibilities for the manipulation and reconstruction of these important chemical structures.



## INTRODUCTION

Polycyclic aromatic hydrocarbons (PAHs) represent a large class of organic compounds composed of multiple aromatic rings that exist naturally in coal, crude oil, and gasoline.<sup>1</sup> The breaking of aromatic rings followed by the reconstruction of covalent C–C bonds in PAHs leads to the production of lighter products with low viscosity and coking tendency, which is an important step in the production of fuels and other chemicals from crude oil.<sup>2</sup> In addition, the breaking of aromatic rings within PAHs in biological systems can lead to the production of easily degradable metabolites or to the conversion of biomass into biofuels.<sup>3,4</sup> However, the covalent aromatic rings in PAHs, including benzenoid structures (e.g., acenes) and non-benzenoid moieties (e.g., azulene), are known for their exceptional stability and resistance to breakdown due to the strong aromaticity.<sup>5</sup> In the crude oil refining industry, the predominant method for breaking aromatic rings involves the hydrogen addition approach, which requires substantial amounts of high-pressure hydrogen.<sup>2,6</sup> Alternatively, using inexpensive oxygen from air as an oxidant in the oxidative ring-opening strategy offers a potential substitute for conventional practices.<sup>2,7</sup> However, these methods often necessitate harsh reaction conditions and suffer from poor selectivity, resulting in the production of multiple undesired byproducts. While enzymes in nature have found ways to break aromatic rings into biofuels or less harmful metabolites in biological systems, it remains difficult to establish the enzymatic environment artificially.<sup>3,8</sup> Furthermore, in recent years,

dearomatic C–C bond cleavage catalyzed by homogeneous transition-metal complexes has emerged as a powerful tool in synthetic organic chemistry.<sup>9–11</sup> Nonetheless, one of the main concerns associated with homogeneous systems lies in the troublesome separation and purification of the products due to the residual catalyst and the presence of impurities.

Apart from the solution chemistry, the C–C bond within aromatic systems can also be disrupted on metal surfaces.<sup>12</sup> With the technique advances in submolecular resolution imaging such as scanning tunneling microscopy (STM) and noncontact atomic force microscopy (nc-AFM), molecular-level insights into on-surface chemical reactions can be obtained through real-space imaging.<sup>13–16</sup> There have been several examples of observing aromatic C–C bond breaking on metal surfaces using STM and nc-AFM. For instance, the breakage of a C<sub>60</sub> cage into graphene quantum dots on Ru(0001) could be achieved at extremely high temperatures (~800 K).<sup>17</sup> Similarly, the C–C bond in an aromatic pentaindenocorannulene could also be broken at an elevated temperature of ~500 K on the Cu(100) surface.<sup>18</sup> Other example include the deconstruction of the aromatic porphyrin via conformational distortion on the

Received: October 19, 2023

Revised: December 6, 2023

Accepted: December 11, 2023

Published: December 23, 2023



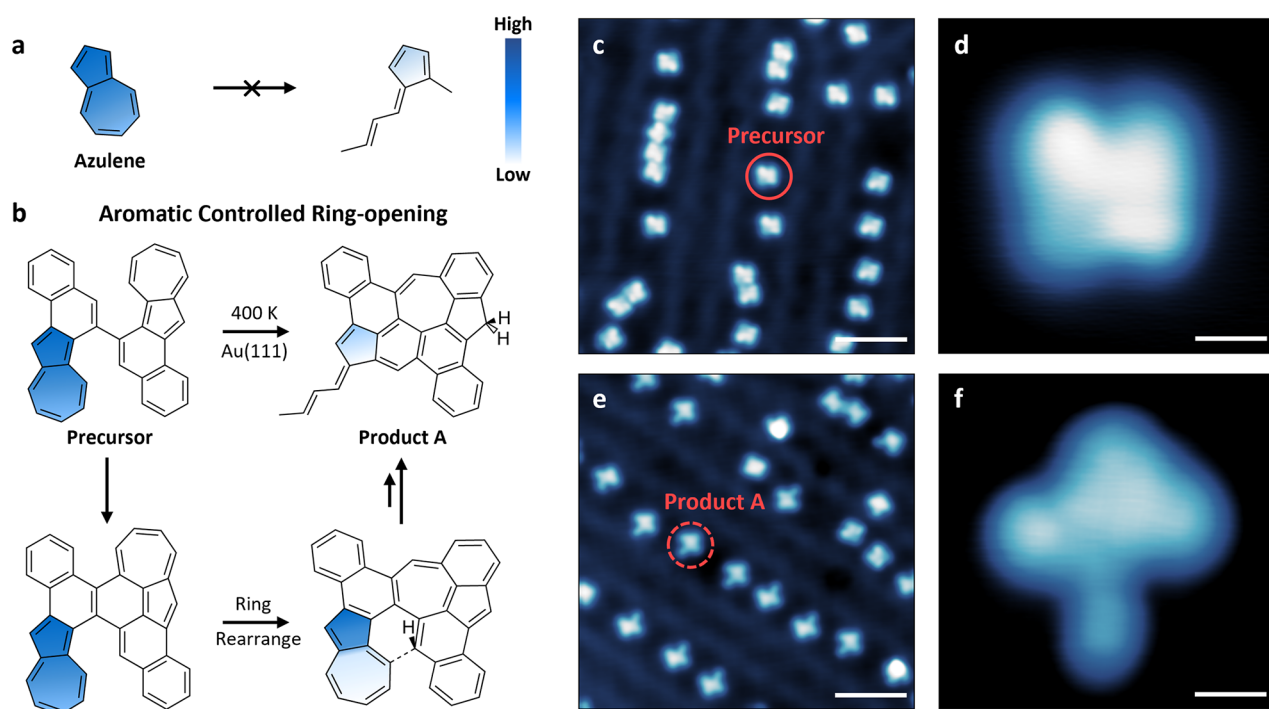


**Figure 1.** Aromaticity-modulated ring-opening of azulene moieties. (a, b) Schematic illustration of the aromaticity-driven ring-opening of the azulene moiety. The blue color bar represents the level of aromaticity of the rings. (c) Large-scale STM image of the precursor molecule deposited on Au(111) before thermal annealing ( $V = 0.05$  V,  $I = 50$  pA). (d) Magnified high-resolution STM image of an individual precursor ( $V = 0.05$  V,  $I = 300$  pA). (e) Large-scale STM image of the products on Au(111) after thermal annealing at 400 K ( $V = 0.05$  V,  $I = 50$  pA). An individual dominant product is highlighted by a red circle. (f) Magnified high-resolution STM image of an individual major product A ( $V = 0.05$  V,  $I = 50$  pA). Scale bars in panels c and e are 4 nm, and in panels d and f are 5 Å.

Cu(111) surface, while the C–C bond was broken as the result of the pyrrole removal.<sup>19</sup> To date, most C–C bond-breaking cases either occur under harsh conditions or involve strained bucky aromatic macrocycles. Interestingly, an exception exists with the fully halogenated aromatic  $C_6Br_6$ , which can be opened to a  $C_6$  polynic chain via a fully debromineative ring-opening process on Ag(111) and ultimately polymerizes into the organometallic polyyne.<sup>20</sup> STM tip manipulation could also reversibly rearrange the C–C bond of aromatic rings in halogenated PAHs through Bergman cyclization.<sup>21,22</sup> However, a direct opening of relatively small nonhalogenated aromatic rings in PAHs with high selectivity and under mild conditions remains elusive.

In this study, we demonstrate a novel strategy for a highly selective on-surface ring-opening of the seven-membered ring (7MR) in azulene moieties. Azulene, a classic non-benzenoid PAH, consists of a pair of fused five- and seven-membered rings,<sup>23,24</sup> where according to Hückel's rule, one  $\pi$  electron of the seven-membered ring can resonate to the five-membered ring, making both rings aromatic with six  $\pi$  electrons.<sup>25</sup> Azulene exhibits the capability of undergoing ring rearrangement to form its isomers, namely, naphthalene and methylene-indene.<sup>16</sup> Nevertheless, direct ring-opening of the azulene via breaking the covalent C–C bond is extremely challenging (Figures 1a and S1).<sup>16,26</sup> Here, we demonstrate that these challenges can be overcome by a stepwise dearomatization strategy coupled with strain-induced internal ring rearrangement and cyclodehydrogenation. As shown in Figure 1b, the precursor chosen here consists of two azulene moieties located at the edges (bottom left and top right) of the molecule. The two fragments containing one azulene moiety are connected by a flexible C–C single bond. Upon annealing, intramolecular fusion via

dehydrogenative cyclization leads to a more extensive conjugation system with decreased molecular height and strain. After that, the upper fused azulene moiety undergoes ring rearrangement to further alleviate internal strain and enhance the orbital overlap with the metal surface,<sup>27–29</sup> which also results in a reduction of the distance between the lower azulene moiety and the rest of the carbon skeleton. This reduced distance enables the possibility of a further fusion of the molecule (indicated by the dashed line in Figure 1b). Through this process, the aromaticity of the 7MR in the lower azulene moiety reaches a local minimum, leading to a noticeable decrease in stability and facilitating the selective ring-opening.

## RESULTS AND DISCUSSION

**Structural Characterization of the Precursor and Products.** The precursor [6,6'-binaphtho[2,1-*a*]azulene] (Figure 1b) was synthesized via multiple synthetic steps (see Methods in the Supporting Information) and then deposited onto Au(111) held at room temperature under ultrahigh vacuum (UHV) conditions. Upon inspection through STM imaging, the Au(111) surface was found to be decorated with square-shaped molecular species (Figure 1c). The magnified STM image (Figure 1d) shows that the precursor molecule exhibits bright features on the upper left and bottom right corners, which are attributed to the tilted molecular configuration due to steric hindrance after adsorption on the surface. It is observed that the bright features on two corners are not identical. When the precursor was deposited onto the surface, variations in relative adsorption sites led to differences in the heights of the tilted-up parts within the molecule (as depicted in Figure S2b,d). Consequently, this disparity in structure height

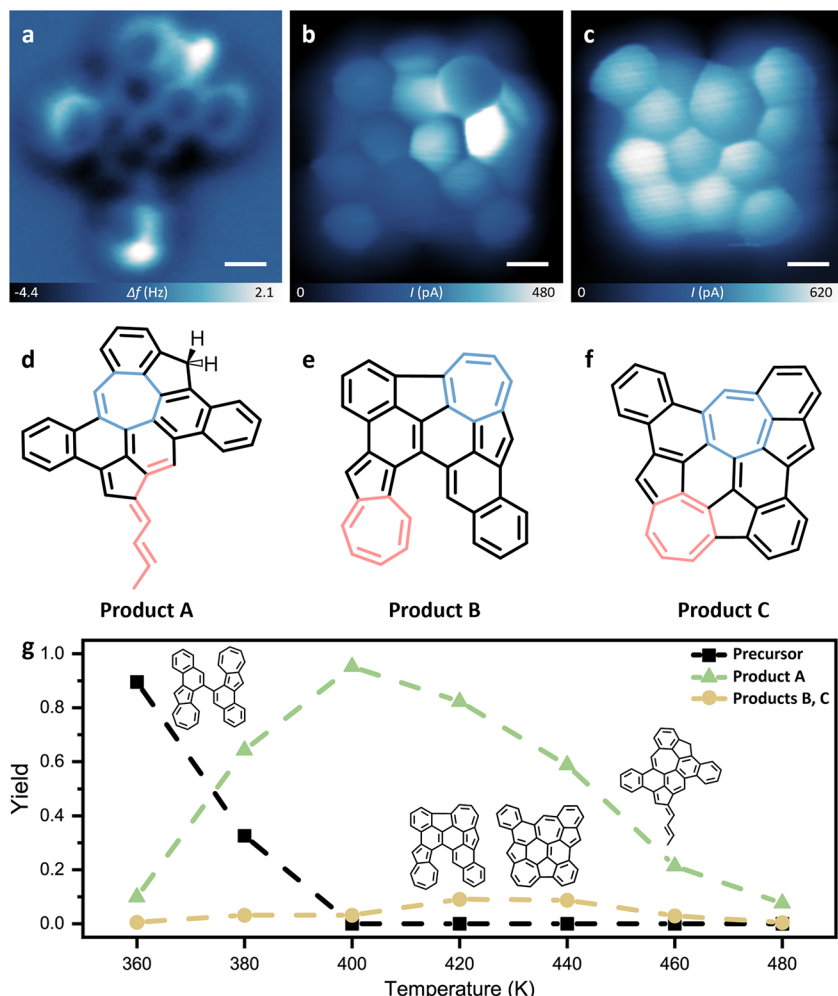


**Figure 2.** Structural characterization of the products. (a) High-resolution nc-AFM image of the major product A acquired with a CO-functionalized tip, collected at tip–sample distance  $z = -135$  pm with respect to set point  $V = 50$  mV,  $I = 50$  pA. (b, c) Bond-resolved STM images of the products B and C acquired with a CO-functionalized tip, respectively. Collected at tip–sample distances  $z = -50$  pm (b) and  $z = -70$  pm (c) with respect to set point  $V = 10$  mV,  $I = 200$  pA. (d–f) Chemical structures of products A, B, and C, respectively. The blue and red colors indicate the positions of the two seven-membered rings in all products. (g) A statistical analysis of the yield of three products at different temperatures. Scale bars in panel a is 4 Å, and in panels b and c are 2 Å.

results in varying levels of brightness in the constant-current STM image. Subsequently, the annealing of the Au(111) substrate at 400 K for 20 min triggered surface-assisted reactions toward the formation of a dominant tree-shaped product A, along with several molecular species displaying different STM contrasts (Figure 1e). The magnified STM image (Figure 1f) suggests that the product A has a relatively planar geometry, as there is no strong contrast present.

We then employed nc-AFM<sup>30–32</sup> and bond-resolved scanning tunneling microscopy (BRSTM)<sup>33–35</sup> measurements to identify the chemical structures for the major product A (Figure 2a) and for the minor products B and C (Figure 2b,c), respectively. The nc-AFM/BRSTM imaging was performed in constant-height mode within the Pauli repulsion regime. In this regime, the CO molecule experiences lateral relaxation in regions of high electron density—chemical bonds, which modulates the frequency shift ( $\Delta f$ ) or conductance in the tunneling junction, resulting in distinct features that correspond to the chemical bond in the frequency shift and tunneling current channel.<sup>36,37</sup> The sharp features associated with the chemical bonds in the nc-AFM and BRSTM images help to distinguish the different ring species (five-, six-, seven-membered rings) clearly. The back-

bone-like features as captured in Figure 2a–c enable us to identify the chemical structures of all products.

The major product A consists of fused five-, six-, and seven-membered rings, along with a trans C–C chain featuring alternating single–double bonds connected at the lower pentagon. Besides, the simulated nc-AFM image of product A (Figure S3) reproduces all the observed key features, further supporting the proposed chemical structure. A direct comparison of the chemical structures of the precursor (Figure 1b) and product A reveals that the trans C–C chain was formed as a result of the ring-opening of the lower seven-membered ring (red color coding in Figure 2d) in the precursor. Additionally, ring rearrangement was observed for the upper seven-membered ring (blue color coding in Figure 2d), apart from the ring-opening. It is worth noting that the bright feature observed in the nc-AFM image of the product A (Figure 2a) suggests that the upper pentagon has a CH<sub>2</sub> termination.<sup>38,39</sup> By contrast, the seven-membered rings of product B remain unopened and unrearranged (Figure 2e), while the upper seven-membered ring of product C undergoes ring rearrangement (blue color coding in Figure 2f). The detailed reaction mechanism will be discussed in the next section.

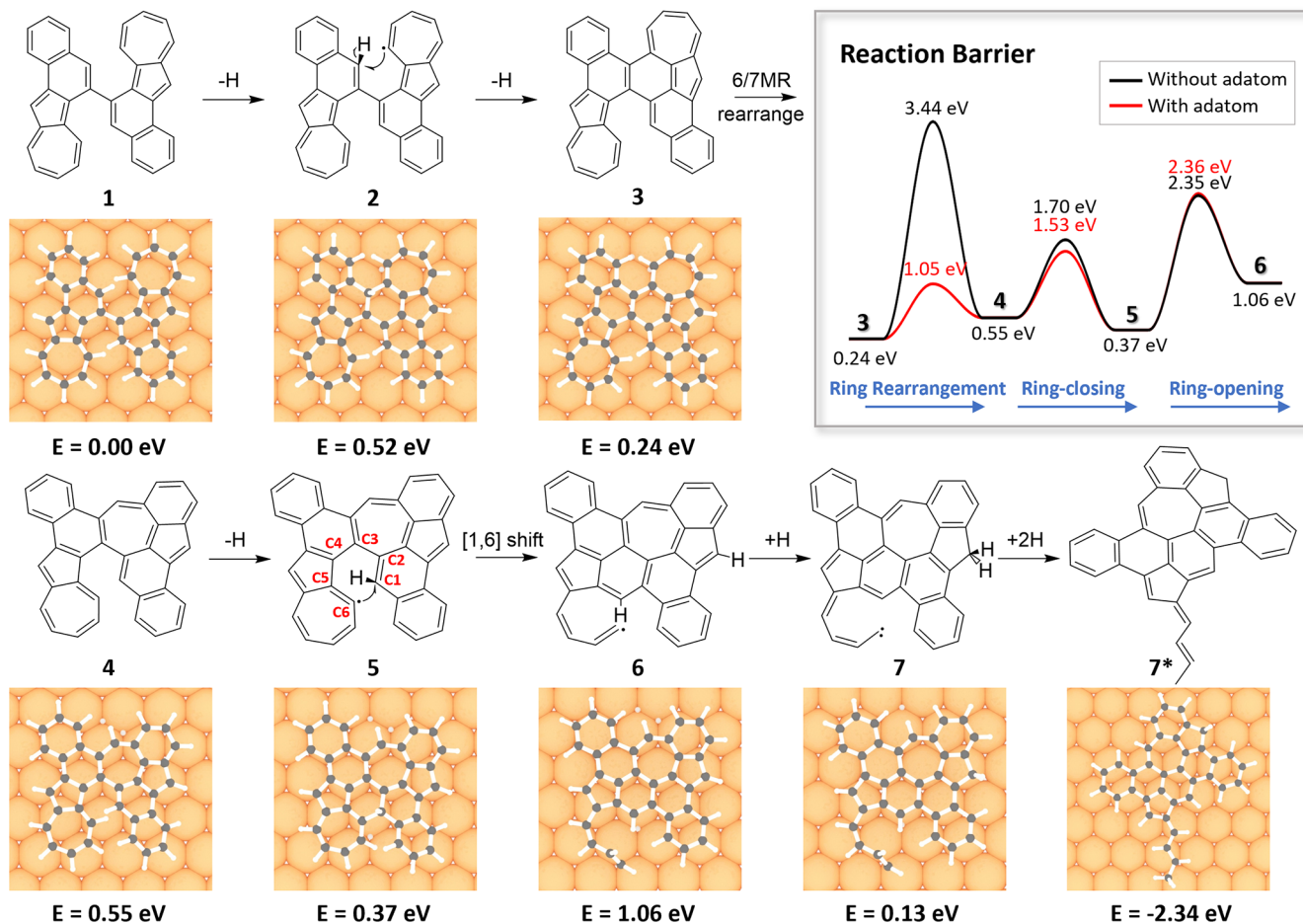


**Figure 3.** Schematic reaction pathway for the formation of the major product A ( $7^*$ ). The chemical structures are followed by the top view of DFT-optimized 3D structures and their corresponding energies. The inset depicts the energy profiles for the key reaction steps, comparing systems with or without a Au adatom. Note: For the adatom cases, the reaction barriers are presented regarding the energies of their initial states (not the global relative energies).

The statistical distribution of these different products was analyzed by examining multiple STM images acquired at temperature increments of 20 K, ranging from 360 to 480 K (Figures 2g and S4). It was observed that the ring-opening of the aromatic azulene could be initiated at 360 K, resulting in a conversion of 10% of the precursor into product A. At 400 K, the precursor was entirely transformed into several products, with the abundance of the major product A reaching a maximum yield of around 95%. However, between 400 and 480 K, the amount of the products decreases with the increase of temperature due to the cross-coupling, resulting in randomly coupled oligomers being present on the surface (Figure S4c–g). It is worth noting that the amounts of products B and C were consistently low at all temperatures, indicating that they are both kinetically and thermodynamically more unfavorable than the major product A.

**Exploration of Reaction Pathway.** Our experimental observations reveal a specific ring-opening process for the azulene moiety within a PAH. Subsequently, we conducted density functional theory (DFT) calculations to provide further insight into this process. As shown in Figure 2d, two key steps are involved in transforming the precursor into the product A: the ring rearrangement of one seven-membered ring and ring-opening of the other. It is worth noting that the two reaction sites are located at two remote corners of the molecule, making the simultaneous occurrence of these two steps unlikely. Instead,

they are expected to occur sequentially. However, it remains unclear which step occurs first, while capturing this information with BRSTM/nc-AFM alone proves to be challenging.

To investigate the intricate reaction mechanism, three potential pathways with varying reaction orders have been proposed (as illustrated in Figure S5). In pathway 1, the ring rearrangement ( $3 \rightarrow 4$ ) occurs first followed by the further fusion of the molecule ( $4 \rightarrow 5$ ) and the opening of the 7MR ( $5 \rightarrow 6$ ). In pathway 2, the molecule undergoes further fusion ( $3 \rightarrow 8$ ), followed by the ring-opening ( $8 \rightarrow 9$ ) and subsequent ring rearrangement ( $9 \rightarrow 6$ ). In contrast to pathways 1 and 2, pathway 3 incorporates the step of ring rearrangement ( $8 \rightarrow 5$ ) between the ring-closing ( $3 \rightarrow 8$ ) and ring-opening ( $5 \rightarrow 6$ ) steps. The red, yellow, and blue shadows in Figure S5 represent the ring rearrangement, ring-closing, and ring-opening steps, respectively. The reaction barriers of the key steps in these three reaction pathways were evaluated by DFT calculations (see Methods).<sup>40,41</sup> The energy profiles and geometries of all intermediates and transition states are provided in Figure S6 and Figures S7–S9, respectively.

Based on the energy profiles provided in Figure S6, the reaction barriers for the ring-closing steps (yellow shadows in Figure S5) show no significant differences. Pathway 1 ( $4 \rightarrow 5$ ) exhibits a barrier of 1.15 eV, while pathways 2 and 3 ( $3 \rightarrow 8$ ) have a slightly higher barrier of 1.47 eV. Similarly, the differences in the reaction barriers for the ring-opening steps (blue shadows

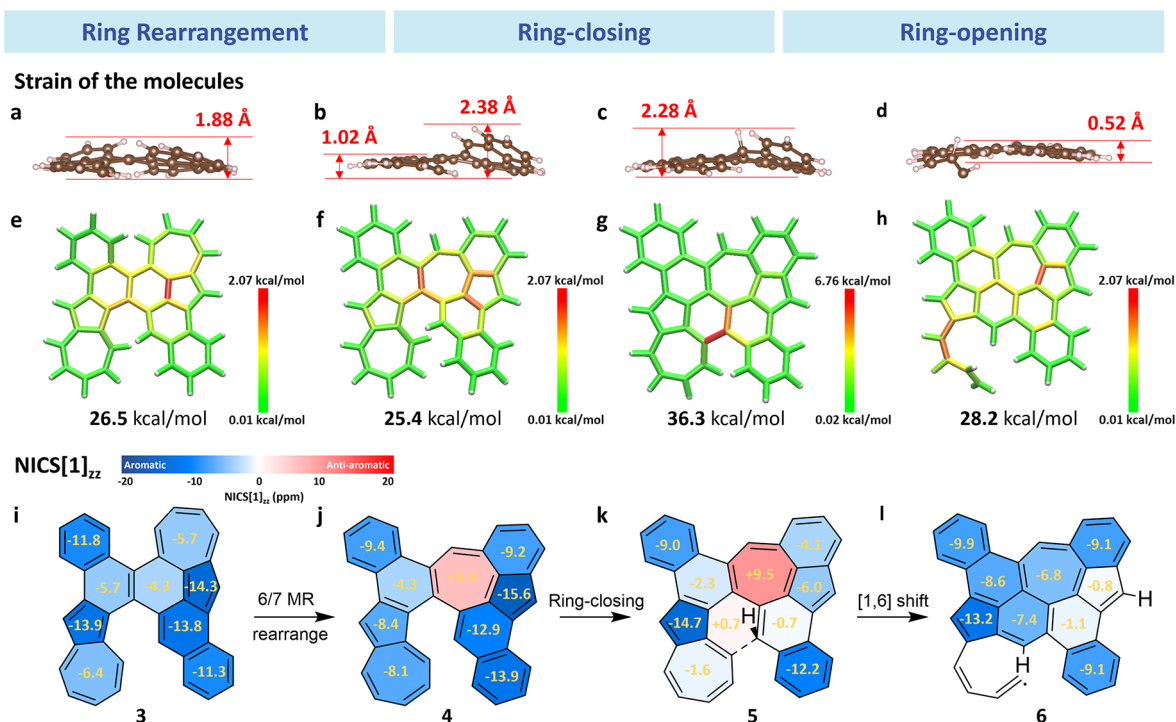


**Figure 4.** (a–d) Optimized adsorption geometries of the reaction intermediates **3**, **4**, **5**, and **6** on the Au(111) surface, respectively. (e–h) Strain distribution and total strain of the reaction intermediates **3**, **4**, **5**, and **6**, respectively. Red/green color represents the strain of a specific bond. (i–l) NICS[1]<sub>zz</sub> of the reaction intermediates **3**, **4**, **5**, and **6**, respectively. The blue and red colors indicate high and low aromaticity, respectively.

in Figure S5) among the three proposed pathways are negligible, with 1.98 eV for pathways 1 and 3 (**5** → **6**) and 1.67 eV for pathway 2 (**8** → **9**). However, significant differences are observed in the reaction barriers for the ring rearrangement steps (red shadows in Figure S5), which have relatively higher barriers than those of the ring-closing and ring-opening steps. The ring rearrangement barrier is predicted to be 3.20 eV for pathway 1 (**3** → **4**), 4.08 eV for pathway 2 (**9** → **6**), and 5.99 eV for pathway 3 (**8** → **5**), respectively. Based on the DFT-calculated energy profiles (Figure S6), pathway 1, with the lowest reaction barrier, is identified as the most probable mechanism for the formation of product A.

The detailed reaction steps and the corresponding energies of all structures in pathway 1 are shown in Figure 3. Initially, one 7MR of the precursor (**1**) undergoes the dehydrogenation and C–C coupling processes (**1** → **2**). Further dehydrogenation results in the formation of intermediate **3**. Subsequently, ring rearrangement of the upper 7MR with its neighboring six-membered ring (6MR) leads to the formation of intermediate **4**. The molecule then undergoes fusion via a ring-closing step (**4** → **5**), which is followed by a H-shift from C1 to C6 in structure **5**, leading to the breaking of the bottom 7MR (**5** → **6**). As shown in Figure S10, structure **6** has a resonance structure **6'** with two unpaired electrons in the terminus of the C–C chain resulting from the broken 7MR and another unpaired electron on the upper five-membered ring (5MR). According to Clar's rule,<sup>42</sup> **6'** is preferred over **6**, as it possesses three additional aromatic sextets, providing extra resonance energy that stabilizes the molecule. The unpaired electron on the upper 5MR can be quenched by a free H in the UHV chamber, generating structure **7**. The CH<sub>2</sub>-terminated upper 5MR in structure **7** corresponds to the bright feature observed in the nc-AFM image (Figure 2a). To quench the other unpaired electrons in the C–C chain terminal, H absorption (to form **7\***/product A) and bonding

with the metal surface are both feasible. In addition, the radicals in **7** could also lead to intermolecular coupling, as shown in Figure S4c–g.

We further introduce a surface adatom to the key reaction steps (refer to Figure S11 for structures of all intermediates and their transition states with adatoms), as they are well-recognized to play an important role in various on-surface reaction processes<sup>43–46</sup> and lower the reaction barrier significantly.<sup>47–49</sup> As shown in the inset of Figure 3, the reaction barrier of the ring rearrangement process in the presence of the Au adatom is 0.81 eV, which is significantly lower than the barrier without the Au adatom (3.20 eV). However, introducing the Au adatom does not substantially impact the reaction barriers of the ring-closing and ring-opening processes. This is likely because the ring rearrangement occurs in the periphery of the molecule, where the adatom can easily approach the activated C without disturbing the adsorption geometry (Figure S11a). On the other hand, the ring-closing and ring-opening occur at the internal part of the molecule, making it difficult for the adatom to approach. In such cases, the adatoms tend to push the molecules upward and make them more distorted, even if they can successfully approach the internal reaction sites (Figure S11b,c).

Even with the inclusion of an adatom, which decreases the barrier for the ring rearrangement to 0.81 eV, the most significant barrier for the entire reaction remains substantial at 1.98 eV, attributed to the ring-opening process. While this barrier might appear relatively high for a reaction occurring at 400 K, the reaction rate ( $\Gamma$ ) governs by the formula  $\Gamma = \nu \times e^{-\Delta F/kT}$ , where  $\Delta F$  represents the free energy barrier,  $T$  is the temperature,  $k$  stands for Boltzmann's constant, and  $\nu$  signifies the effective frequency associated with vibrations aligned with the reaction path.<sup>50</sup> As shown in Figure S12, there are 16 effective vibrational modes, arising from the high molecular internal strain, aligned with the ring-opening reaction

path. These modes could contribute to an increased reaction rate and enable the system to overcome the barrier.<sup>43,45</sup>

**Investigation of the Reaction Driving Force.** Although pathway 1 has been identified as the most probable mechanism, the underlying driving force of the key steps, namely, ring rearrangement ( $3 \rightarrow 4$ ), ring-closing ( $4 \rightarrow 5$ ), and ring-opening ( $5 \rightarrow 6$ ), remains unknown. Hence, we have conducted calculations involving geometry, strain,<sup>51</sup> and nucleus-independent chemical shift (NICS)<sup>52,53</sup> to analyze each of these key reaction steps. The results of these analyses are summarized in Figure 4 for the key intermediates 3, 4, 5, and 6. Furthermore, the molecular height and strain changes between these intermediates are plotted in Figure S13.

As shown in Figure 4a,b,e,f, for the ring rearrangement ( $3 \rightarrow 4$ ) step, the intramolecular strain of intermediate 4 is reduced by 1.1 kcal/mol compared to intermediate 3. Accordingly, it becomes partially more planar. Consequently, the ring rearrangement of the 6/7MR is facilitated by the release of internal strain and the improvement in orbital overlapping between the molecule and surface, particularly in a planar configuration.<sup>27–29</sup> To investigate the molecular aromaticity, NICS calculations were performed. A negative NICS value indicates that the ring is aromatic, while a positive value indicates antiaromaticity. The strength of aromaticity increases as the value becomes more negative, and *vice versa*.<sup>52,53</sup> The rearranged 7MR in intermediate 4 becomes antiaromatic (Figure 4i,j). This occurs because the ring rearrangement weakens the electronic communication between the 5MR and 7MR in the upper azulene moiety.

Following the ring rearrangement, the ring-closing step ( $4 \rightarrow 5$ ) occurs, resulting in further fusion of the molecule. The tilted-up H in intermediate 5 increases the intramolecular stain (36.3 kcal/mol) significantly (Figure 4f,g). However, as a new chemical bond is formed (indicated by the dashed line of intermediate 5 in Figure 4k), the NICS value of the lower 7MR increases dramatically to -1.6. This high NICS value suggests the nonaromatic nature of this 7MR. Consequently, the aromaticity of the lower 7MR reaches a local minimum, and together with the strong molecular internal strain, this 7MR becomes less stable and more prone to further ring-opening.

Last but not least, the shifting of H (tilted in intermediate 5) from C1 to C6 (Figure 3) triggers the opening of the nonaromatic 7MR in the lower azulene moiety. As shown in Figure 4d,h, the resulting ring-opening product 6 adopts a more planar structure (deviating by 1.76 Å) and lower internal strain (8.1 kcal/mol lower than that of 5). Similar to the ring rearrangement step, the ring-opening step is facilitated by the release of internal strain and the improvement in orbital overlapping between the molecule and surface. In contrast to the presence of two antiaromatic rings in 5, all rings in intermediate 6 are aromatic (Figure 4l). Based on a thorough analysis of the computational results, it can be concluded that the ring-opening of the aromatic azulene moiety could be facilitated by a stepwise approach that involves manipulating the molecular internal strain and local aromaticity.

To gain a deeper understanding of the chemical reactions under realistic conditions at elevated temperatures, we have also performed the adatom-participating quantum mechanics/molecular mechanics (QM/MM) calculations at 400 K (see Methods).<sup>54,55</sup> As evidenced in Figure S14, the bond length of the to-be-broken C–C bond in 5 (~1.53 Å) is longer than that in 4 (~1.45 Å), indicating the ring-closing step ( $4 \rightarrow 5$ ) weakens the specific chemical bond and further promotes its subsequent

breakage. Furthermore, the QM/MM method was employed to calculate the ring-opening reaction barrier at 400 K, which was determined to be 2.26 eV (Figure S15). This value is comparable with the previous adatom-participating DFT calculation (1.99 eV). A video showcasing the reaction process is provided in the Supporting Information.

**Comparison of Precursor and Various Products.** Based on pathway 1 and the chemical structures of products B and C, we propose the reaction pathways for their formation (Figure S16). The DFT-optimized 3D structures and the corresponding energies for the two reaction pathways are summarized in Figure S17. As shown in Figure S16, instead of 6/7MR rearrangement, the formation of product B ( $3 \rightarrow 10$ ,  $10 \rightarrow 11$ ) arises from further cyclodehydrogenation (CDH) from structure 3. In contrast to the H-shaped intermediate 3, the fused upper backbone (11, product B) makes the distance between the two lower skeletons larger (like A-shape) and forbids their further CDH (Figure S17a). The observation of product B without further ring-opening of 7MR in the azulene moiety also indicates that the ring arrangement ( $3 \rightarrow 4$ ) plays an essential role in promoting the further ring-closing ( $4 \rightarrow 5$ ) by reducing the distance between the two lower skeletons. Moreover, if the tilted H does not shift from C1 to C6 in the ring-opening step ( $5 \rightarrow 6$ ) but drops to the surface ( $5 \rightarrow 12$ ), the product C can be obtained through further CDH ( $12 \rightarrow 13$ ,  $13 \rightarrow 14$  in Figures S16 and S17b). The observations of product B and C also support the reliability of the proposed reaction mechanism of major product A. A detailed discussion of product B and C formation mechanisms can be found in the Supplementary Note.

Investigations have also been carried out to analyze the contributions of molecular strain and aromaticity in the reactions occurring from the precursor to all resulting products (Figure S18). Notably, the height and total strain of all products are lower than that of the precursor (Figure S18a–h). This observation suggests that the enhancement of molecule–surface overlapping and the reduction of intramolecular strain are the key driving forces in the chemical process occurring on the surface. Among the products, product C exhibits the lowest total strain owing to its almost planar structure with the minimum height. In the case of the product A, its height is comparatively larger due to the presence of the tilted hydrogens of the CH<sub>2</sub> in the upper 5MR and methyl terminal in the C–C chain. However, its total strain is also quite small, likely attributed to its planar conjugated carbon backbone (Figure S18b).

The on-surface reactions have also modulated the aromaticity of different portions within the final products (Figure S18i–l). Significant aromaticity changes exist between the precursor and product A after the above-mentioned reaction. The upper rearranged 7MR in product A exhibits antiaromaticity due to the limited electronic communication between the upper 5/7MR in the azulene moiety. The lower 5MR in product A displays weaker aromaticity compared to its counterpart in the precursor due to the loss of its original paired 7MR in the lower azulene moiety. It should be noted that the ring-opening process to form product A can only be achieved by manipulating local aromaticity during the on-surface reaction ( $5 \rightarrow 6$ ). In contrast to the significant aromaticity changes in product A, neither ring rearrangement nor ring-opening occurred in product B, resulting in the aromaticity of the two azulene moieties remaining similar to that of the precursor. In the case of product C, the upper 5MR and the lower 7MR become less aromatic, attributed to the ring rearrangement of the upper

azulene moiety and further fusion of the lower azulene moiety with the other carbon skeleton, respectively.

## CONCLUSION

In this work, we successfully demonstrated a highly selective ring-opening of the seven-membered ring in aromatic azulene moieties on the Au(111) surface. Through bond-resolved scanning probe microscopy, we accurately identified the chemical structures of all resulting products. Furthermore, by employing density functional theory calculations, we elucidated the mechanism underlying the ring-opening process and its chemical driving forces. With the help of a stepwise ring rearrangement and cyclodehydrogenation, the aromaticity within the molecule is modulated. By achieving the local minimum of aromaticity at the seven-membered ring of the azulene moiety, further ring-opening is facilitated. These findings provide valuable insights into the ring-opening of polycyclic aromatic hydrocarbons, which shed light on the manipulation and reconstruction of these aromatic molecules in the field of laboratory-based on-surface chemistry and the oil refining industry.

## ASSOCIATED CONTENT

### Supporting Information

The Supporting Information is available free of charge at <https://pubs.acs.org/doi/10.1021/jacs.3c11652>.

Precursor geometries, theoretical AFM image simulation, supplementary STM data, three proposed reaction pathways, the calculated reaction energy profiles and the reaction intermediate geometries, QM/MM calculation results, discussion of the reaction pathways to form products B and C, experimental and theoretical methods ([PDF](#))

Video of the ring-opening process under QM/MM calculation ([MP4](#))

### Accession Codes

CCDC 2267635 contains the supplementary crystallographic data for this paper. These data can be obtained free of charge via [www.ccdc.cam.ac.uk/data\\_request/cif](http://www.ccdc.cam.ac.uk/data_request/cif), or by emailing [data\\_request@ccdc.cam.ac.uk](mailto:data_request@ccdc.cam.ac.uk), or by contacting The Cambridge Crystallographic Data Centre, 12 Union Road, Cambridge CB2 1EZ, UK; fax: +44 1223 336033.

## AUTHOR INFORMATION

### Corresponding Authors

Jiong Lu – Department of Chemistry, National University of Singapore, 117543, Singapore; Institute for Functional Intelligent Materials, National University of Singapore, 117544, Singapore; [orcid.org/0000-0002-3690-8235](#); Email: [chmluj@nus.edu.sg](mailto:chmluj@nus.edu.sg)

Ming Wah Wong – Department of Chemistry, National University of Singapore, 117543, Singapore; [orcid.org/0000-0003-2162-1220](#); Email: [chmw@nus.edu.sg](mailto:chmw@nus.edu.sg)

Junzhi Liu – Department of Chemistry and State Key Laboratory of Synthetic Chemistry, The University of Hong Kong, 999077 Hong Kong, People's Republic of China; [orcid.org/0000-0001-7146-0942](#); Email: [juliu@hku.hk](mailto:juliu@hku.hk)

Pavel Jelínek – Institute of Physics of the Czech Academy of Science, 16200 Praha, Czech Republic; Regional Centre of Advanced Technologies and Materials, Palacký University, 78371 Olomouc, Czech Republic; [orcid.org/0000-0002-5645-8542](#); Email: [jelinekp@fzu.cz](mailto:jelinekp@fzu.cz)

## Authors

Lulu Wang – Department of Chemistry, National University of Singapore, 117543, Singapore; [orcid.org/0000-0002-2973-0598](#)

Xinnan Peng – Department of Chemistry, National University of Singapore, 117543, Singapore

Jie Su – Department of Chemistry, National University of Singapore, 117543, Singapore; [orcid.org/0000-0003-1071-9556](#)

Junting Wang – Department of Chemistry and State Key Laboratory of Synthetic Chemistry, The University of Hong Kong, 999077 Hong Kong, People's Republic of China

Aurelio Gallardo – Institute of Physics of the Czech Academy of Science, 16200 Praha, Czech Republic

Hui Yang – Department of Chemistry, National University of Singapore, 117543, Singapore

Qifan Chen – Institute of Physics of the Czech Academy of Science, 16200 Praha, Czech Republic

Pin Lyu – Department of Chemistry, National University of Singapore, 117543, Singapore

Complete contact information is available at:

<https://pubs.acs.org/10.1021/jacs.3c11652>

### Author Contributions

#L.W., X.P., J.S., and J.W. contributed equally.

### Notes

The authors declare no competing financial interest.

## ACKNOWLEDGMENTS

J.L. acknowledges the support from the NRF, Prime Minister's Office, Singapore, under the Competitive Research Program Award (NRF-CRP29-2022-0004), MOE Tier 2 grants (MOE-T2EP10221-0005 and MOE-T2EP10123-0004) and Agency for Science, Technology and Research (A\*STAR) under MTC Individual Research Grants (Project ID: M21K2c0113). J.Z.L. is grateful for the funding from the Hong Kong Research Grants Council (27301720, 17304021) and National Natural Science Foundation of China (22122114). P.J., A.G., and Q.C. appreciate funding from the GACR 20-13692X and the CzechNanoLab Research Infrastructure supported by MEYS CR (LM2023051). J.S. acknowledges the support from Agency for Science, Technology and Research (A\*STAR) Advanced Manufacturing & Engineering (AME) Young Individual Research Grant (YIRG) A2084c0171. L.W. thanks Applied Materials-NUS Advanced Materials Corporate Lab for the Ph.D. scholarship.

## REFERENCES

- (1) Lawal, A. T. Polycyclic aromatic hydrocarbons. A review. *Cogent Environmental Science* **2017**, *3*, 1339841.
- (2) Sánchez, N. M.; de Klerk, A. Heavy Oil Upgrading by Oxidative Ring-Opening of Polycyclic Aromatic Hydrocarbons. In *Catalytic and Noncatalytic Upgrading of Oils*; ACS Symposium Series, Vol. 1379; American Chemical Society, 2021; pp 189–209.
- (3) Stading, R.; Gastelum, G.; Chu, C.; Jiang, W.; Moorthy, B. Molecular mechanisms of pulmonary carcinogenesis by polycyclic aromatic hydrocarbons (PAHs): Implications for human lung cancer. *Seminars in Cancer Biology* **2021**, *76*, 3–16.
- (4) Morya, R.; Salvachúa, D.; Thakur, I. S. Burkholderia: An Untapped but Promising Bacterial Genus for the Conversion of Aromatic Compounds. *Trends Biotechnol.* **2020**, *38*, 963–975.
- (5) Aihara, J.-i. Why aromatic compounds are stable. *Sci. Am.* **1992**, *266*, 62–69.

- (6) Weitkamp, J. Catalytic Hydrocracking—Mechanisms and Versatility of the Process. *ChemCatChem.* **2012**, *4*, 292–306.
- (7) Montoya Sánchez, N.; de Klerk, A. Oxidative Ring-Opening of Aromatics: Decomposition of Biphenyl Carboxylic Acids and Zinc Biphenyl Carboxylates. *Energy Fuels* **2015**, *29*, 7910–7922.
- (8) Guengerich, F. P.; Yoshimoto, F. K. Formation and Cleavage of C–C Bonds by Enzymatic Oxidation-Reduction Reactions. *Chem. Rev.* **2018**, *118*, 6573–6655.
- (9) Sattler, A.; Parkin, G. Cleaving carbon-carbon bonds by inserting tungsten into unstrained aromatic rings. *Nature* **2010**, *463*, 523–526.
- (10) Hu, S.; Shima, T.; Hou, Z. Carbon-carbon bond cleavage and rearrangement of benzene by a trinuclear titanium hydride. *Nature* **2014**, *512*, 413–415.
- (11) Qiu, X.; Sang, Y.; Wu, H.; Xue, X.-S.; Yan, Z.; Wang, Y.; Cheng, Z.; Wang, X.; Tan, H.; Song, S.; Zhang, G.; Zhang, X.; Houk, K. N.; Jiao, N. Cleaving arene rings for acyclic alkenynitrile synthesis. *Nature* **2021**, *597*, 64–69.
- (12) Clair, S.; de Oteyza, D. G. Controlling a Chemical Coupling Reaction on a Surface: Tools and Strategies for On-Surface Synthesis. *Chem. Rev.* **2019**, *119*, 4717–4776.
- (13) Hla, S.-W.; Bartels, L.; Meyer, G.; Rieder, K.-H. Inducing All Steps of a Chemical Reaction with the Scanning Tunneling Microscope Tip: Towards Single Molecule Engineering. *Phys. Rev. Lett.* **2000**, *85*, 2777–2780.
- (14) Pavliček, N.; Schuler, B.; Collazos, S.; Moll, N.; Pérez, D.; Guitián, E.; Meyer, G.; Peña, D.; Gross, L. On-surface generation and imaging of arynes by atomic force microscopy. *Nat. Chem.* **2015**, *7*, 623–628.
- (15) Pavliček, N.; Gawel, P.; Kohn, D. R.; Majzik, Z.; Xiong, Y.; Meyer, G.; Anderson, H. L.; Gross, L. Polyyne formation via skeletal rearrangement induced by atomic manipulation. *Nat. Chem.* **2018**, *10*, 853–858.
- (16) Fan, Q.; Martin-Jimenez, D.; Ebeling, D.; Krug, C. K.; Brechmann, L.; Kohlmeyer, C.; Hilt, G.; Hieringer, W.; Schirmeisen, A.; Gottfried, J. M. Nanoribbons with Nonalternant Topology from Fusion of Polyazulene: Carbon Allotropes beyond Graphene. *J. Am. Chem. Soc.* **2019**, *141*, 17713–17720.
- (17) Lu, J.; Yeo, P. S. E.; Gan, C. K.; Wu, P.; Loh, K. P. Transforming C<sub>60</sub> molecules into graphene quantum dots. *Nat. Nanotechnol.* **2011**, *6*, 247–252.
- (18) Wackerlin, C.; Gallardo, A.; Mairena, A.; Baljzović, M.; Cahlik, A.; Antalík, A.; Brabec, J.; Veis, L.; Nachtigallova, D.; Jelínek, P.; Ernst, K.-H. On-Surface Hydrogenation of Buckybowls: From Curved Aromatic Molecules to Planar Non-Kekulé Aromatic Hydrocarbons. *ACS Nano* **2020**, *14*, 16735–16742.
- (19) Bischoff, F.; Riss, A.; Michelitsch, G. S.; Ducke, J.; Barth, J. V.; Reuter, K.; Auwärter, W. Surface-Mediated Ring-Opening and Porphyrin Deconstruction via Conformational Distortion. *J. Am. Chem. Soc.* **2021**, *143*, 15131–15138.
- (20) Gao, W.; Kang, F.; Qiu, X.; Yi, Z.; Shang, L.; Liu, M.; Qiu, X.; Luo, Y.; Xu, W. On-Surface Debromination of C<sub>6</sub>Br<sub>6</sub>: C<sub>6</sub> Ring versus C<sub>6</sub> Chain. *ACS Nano* **2022**, *16*, 6578–6584.
- (21) Schuler, B.; Fatayer, S.; Mohn, F.; Moll, N.; Pavliček, N.; Meyer, G.; Peña, D.; Gross, L. Reversible Bergman cyclization by atomic manipulation. *Nat. Chem.* **2016**, *8*, 220–224.
- (22) Albrecht, F.; Fatayer, S.; Pozo, I.; Tavernelli, I.; Repp, J.; Peña, D.; Gross, L. Selectivity in single-molecule reactions by tip-induced redox chemistry. *Science* **2022**, *377*, 298–301.
- (23) Huang, J.; Huang, S.; Zhao, Y.; Feng, B.; Jiang, K.; Sun, S.; Ke, C.; Kymakis, E.; Zhuang, X. Azulene-Based Molecules, Polymers, and Frameworks for Optoelectronic and Energy Applications. *Small Methods* **2020**, *4*, 2000628.
- (24) Xin, H.; Hou, B.; Gao, X. Azulene-Based π-Functional Materials: Design, Synthesis, and Applications. *Acc. Chem. Res.* **2021**, *54*, 1737–1753.
- (25) Hückel, E. Quanstentheoretische Beiträge zum Benzolproblem. *Zeitschrift für Physik* **1931**, *72*, 310–337.
- (26) Sun, Q.; Hou, I. C.-Y.; Eimre, K.; Pignedoli, C. A.; Ruffieux, P.; Narita, A.; Fasel, R. On-surface synthesis of polyazulene with 2,6-connectivity. *Chem. Commun.* **2019**, *55*, 13466–13469.
- (27) Mallada, B.; de la Torre, B.; Mendieta-Moreno, J. I.; Nachtigallova, D.; Matěj, A.; Matoušek, M.; Mutombo, P.; Brabec, J.; Veis, L.; Cadart, T.; Kotora, M.; Jelínek, P. On-Surface Strain-Driven Synthesis of Nonalternant Non-Benzenoid Aromatic Compounds Containing Four- to Eight-Membered Rings. *J. Am. Chem. Soc.* **2021**, *143*, 14694–14702.
- (28) Shiotari, A.; Nakae, T.; Iwata, K.; Mori, S.; Okujima, T.; Uno, H.; Sakaguchi, H.; Sugimoto, Y. Strain-induced skeletal rearrangement of a polycyclic aromatic hydrocarbon on a copper surface. *Nat. Commun.* **2017**, *8*, 16089.
- (29) Su, J.; Wu, X.; Song, S.; Telychko, M.; Lu, J. Substrate induced strain for on-surface transformation and synthesis. *Nanoscale* **2020**, *12*, 7500–7508.
- (30) Gross, L.; Mohn, F.; Moll, N.; Liljeroth, P.; Meyer, G. The Chemical Structure of a Molecule Resolved by Atomic Force Microscopy. *Science* **2009**, *325*, 1110–1114.
- (31) Gross, L. Recent advances in submolecular resolution with scanning probe microscopy. *Nat. Chem.* **2011**, *3*, 273–278.
- (32) Telychko, M.; Li, G.; Mutombo, P.; Soler-Polo, D.; Peng, X.; Su, J.; Song, S.; Koh, M. J.; Edmonds, M.; Jelínek, P.; Wu, J.; Lu, J. Ultrahigh-yield on-surface synthesis and assembly of circumcoronene into a chiral electronic Kagome-honeycomb lattice. *Science Advances* **2021**, *7*, No. eabf0269.
- (33) Nguyen, G. D.; Tsai, H.-Z.; Omrani, A. A.; Marangoni, T.; Wu, M.; Rizzo, D. J.; Rodgers, G. F.; Cloke, R. R.; Durr, R. A.; Sakai, Y.; Liou, F.; Aikawa, A. S.; Chelikowsky, J. R.; Louie, S. G.; Fischer, F. R.; Crommie, M. F. Atomically precise graphene nanoribbon heterojunctions from a single molecular precursor. *Nat. Nanotechnol.* **2017**, *12*, 1077–1082.
- (34) Peng, X.; Mahalingam, H.; Dong, S.; Mutombo, P.; Su, J.; Telychko, M.; Song, S.; Lyu, P.; Ng, P. W.; Wu, J.; Jelínek, P.; Chi, C.; Rodin, A.; Lu, J. Visualizing designer quantum states in stable macrocycle quantum corrals. *Nat. Commun.* **2021**, *12*, 5895.
- (35) Song, S.; Guo, N.; Li, X.; Li, G.; Haketa, Y.; Telychko, M.; Su, J.; Lyu, P.; Qiu, Z.; Fang, H.; Peng, X.; Li, J.; Wu, X.; Li, Y.; Su, C.; Koh, M. J.; Wu, J.; Maeda, H.; Zhang, C.; Lu, J. Real-Space Imaging of a Single-Molecule Monoradical Reaction. *J. Am. Chem. Soc.* **2020**, *142*, 13550–13557.
- (36) Hapala, P.; Kichin, G.; Wagner, C.; Tautz, F. S.; Temirov, R.; Jelínek, P. Mechanism of high-resolution STM/AFM imaging with functionalized tips. *Phys. Rev. B* **2014**, *90*, 085421.
- (37) Krejčí, O.; Hapala, P.; Ondráček, M.; Jelínek, P. Principles and simulations of high-resolution STM imaging with a flexible tip apex. *Phys. Rev. B* **2017**, *95*, 045407.
- (38) Pavliček, N.; Mistry, A.; Majzik, Z.; Moll, N.; Meyer, G.; Fox, D. J.; Gross, L. Synthesis and characterization of triangulene. *Nat. Nanotechnol.* **2017**, *12*, 308–311.
- (39) Mishra, S.; Fatayer, S.; Fernández, S.; Kaiser, K.; Peña, D.; Gross, L. Nonbenzenoid High-Spin Polycyclic Hydrocarbons Generated by Atom Manipulation. *ACS Nano* **2022**, *16*, 3264–3271.
- (40) Zeng, Z.; Guo, D.; Wang, T.; Chen, Q.; Matěj, A.; Huang, J.; Han, D.; Xu, Q.; Zhao, A.; Jelínek, P.; de Oteyza, D. G.; McEwen, J.-S.; Zhu, J. Chemisorption-Induced Formation of Biphenylene Dimer on Ag(111). *J. Am. Chem. Soc.* **2022**, *144*, 723–732.
- (41) Kong, H.; Zhang, C.; Sun, Q.; Yu, X.; Xie, L.; Wang, L.; Li, L.; Hu, S.; Ju, H.; He, Y.; Zhu, J.; Xu, W. Nickel Adatoms Induced Tautomeric Dehydrogenation of Thymine Molecules on Au(111). *ACS Nano* **2018**, *12*, 9033–9039.
- (42) Clar, E. *The Aromatic Sextet*; John Wiley, 1972.
- (43) Telychko, M.; Su, J.; Gallardo, A.; Gu, Y.; Mendieta-Moreno, J. I.; Qi, D.; Tadić, A.; Song, S.; Lyu, P.; Qiu, Z.; Fang, H.; Koh, M. J.; Wu, J.; Jelínek, P.; Lu, J. Strain-Induced Isomerization in One-Dimensional Metal-Organic Chains. *Angew. Chem., Int. Ed.* **2019**, *58*, 18591–18597.
- (44) Mendieta-Moreno, J. I.; Mallada, B.; de la Torre, B.; Cadart, T.; Kotora, M.; Jelínek, P. Unusual Scaffold Rearrangement in Polyaromatic Hydrocarbons Driven by Concerted Action of Single Gold

Atoms on a Gold Surface. *Angew. Chem., Int. Ed.* **2022**, *61*, No. e202208010.

(45) de la Torre, B.; Matěj, A.; Sánchez-Grande, A.; Cirera, B.; Mallada, B.; Rodríguez-Sánchez, E.; Santos, J.; Mendieta-Moreno, J. I.; Edalatmanesh, S.; Lauwaet, K.; Otyepka, M.; Medved', M.; Buendía, C.; Miranda, R.; Martín, N.; Jelínek, P.; Écija, D. Tailoring  $\pi$ -conjugation and vibrational modes to steer on-surface synthesis of pentalene-bridged ladder polymers. *Nat. Commun.* **2020**, *11*, 4567.

(46) Lowe, B.; Hellerstedt, J.; Matěj, A.; Mutombo, P.; Kumar, D.; Ondráček, M.; Jelinek, P.; Schiffrian, A. Selective Activation of Aromatic C-H Bonds Catalyzed by Single Gold Atoms at Room Temperature. *J. Am. Chem. Soc.* **2022**, *144*, 21389–21397.

(47) Li, Q.; Yang, B.; Björk, J.; Zhong, Q.; Ju, H.; Zhang, J.; Cao, N.; Shi, Z.; Zhang, H.; Ebeling, D.; Schirmeisen, A.; Zhu, J.; Chi, L. Hierarchical Dehydrogenation Reactions on a Copper Surface. *J. Am. Chem. Soc.* **2018**, *140*, 6076–6082.

(48) Niu, K.; Lin, H.; Zhang, J.; Zhang, H.; Li, Y.; Li, Q.; Chi, L. Mechanistic investigations of the Au catalysed C-H bond activations in on-surface synthesis. *Phys. Chem. Chem. Phys.* **2018**, *20*, 15901–15906.

(49) Björk, J.; Sánchez-Sánchez, C.; Chen, Q.; Pignedoli, C. A.; Rosen, J.; Ruffieux, P.; Feng, X.; Narita, A.; Müllen, K.; Fasel, R. The Role of Metal Adatoms in a Surface-Assisted Cyclodehydrogenation Reaction on a Gold Surface. *Angew. Chem., Int. Ed.* **2022**, *61*, No. e202212354.

(50) Vineyard, G. H. Frequency factors and isotope effects in solid state rate processes. *J. Phys. Chem. Solids* **1957**, *3*, 121–127.

(51) Colwell, C. E.; Price, T. W.; Stauch, T.; Jasti, R. Strain visualization for strained macrocycles. *Chemical Science* **2020**, *11*, 3923–3930.

(52) Schleyer, P. v. R.; Maerker, C.; Dransfeld, A.; Jiao, H.; van Eikema Hommes, N. J. Nucleus-independent chemical shifts: a simple and efficient aromaticity probe. *J. Am. Chem. Soc.* **1996**, *118*, 6317–6318.

(53) Fallah-Bagher-Shaidei, H.; Wannere, C. S.; Corminboeuf, C.; Puchta, R.; Schleyer, P. v. R. Which NICS Aromaticity Index for Planar  $\pi$  Rings Is Best? *Org. Lett.* **2006**, *8*, 863–866.

(54) Lewis, J. P.; Jelínek, P.; Ortega, J.; Demkov, A. A.; Trabada, D. G.; Haycock, B.; Wang, H.; Adams, G.; Tomfohr, J. K.; Abad, E.; Wang, H.; Drabold, D. A. Advances and applications in the FIREBALL ab initio tight-binding molecular-dynamics formalism. *physica status solidi (b)* **2011**, *248*, 1989–2007.

(55) Mendieta-Moreno, J. I.; Walker, R. C.; Lewis, J. P.; Gómez-Puertas, P.; Mendieta, J.; Ortega, J. fireball/amber: An Efficient Local-Orbital DFT QM/MM Method for Biomolecular Systems. *J. Chem. Theory Comput.* **2014**, *10*, 2185–2193.